

# On the validity of the independent pixel approximation for boundary layer clouds observed during ASTEX

Paquita Zuidema and K. Franklin Evans

Program in Atmospheric and Oceanic Sciences, University of Colorado, Boulder

**Abstract.** The two-dimensional radiative transfer behavior of nine marine stratocumulus clouds observed by cloud radar during the Atlantic Stratocumulus Transition Experiment is examined. The cloud radar resolves the vertical structure to 37.5 m. The method of [Frisch *et al.*, 1995] is used to convert radar reflectivities to extinction fields. Three constructions of the same cloud field help elucidate underlying causes of variability: one is fully two-dimensional, while the other two have vertically uniform extinction fields but possess either a flat cloud top or the original cloud top topography. Two-dimensional solar radiative transfer results are compared with the independent pixel approximation (IPA) result.

At the scale of the domain ( $\approx 7$  km) the IPA albedo bias is small, even after including vertical structure. Locally, in contrast, the direct solar beam interaction with cloud top geometry competes with radiative smoothing as the dominant radiative process. Power spectral analysis of nadir reflectances is dominated by radiative smoothing for overhead Sun, and side illumination/shadowing of cloud top bumps for low Sun. A method that incorporates direct beam interactions with the cloud geometry, in addition to radiative smoothing, significantly improves correlations of a smoothed IPA radiance field with the 2-D reflectances. In a remote sensing application, optical depth and albedo retrieval biases from plane-parallel theory depend on the spatial scale chosen to emulate a satellite pixel size. For scales less than a few kilometers and with low Sun, cloud top topography can cause large positive optical depth biases even when averaged over the entire domain. At larger spatial scales the negative IPA bias always dominates. Domain-averaged monochromatic albedo retrieval errors remain below 0.005, a relative error of less than 1%.

## 1. Introduction

Plane-parallel radiative transfer has been known to be inadequate for the modeling of cloudy atmospheres for many years. One example is the inability by climate models to achieve realistic albedos using observed cloud water mass [Harshvardhan *et al.*, 1989]. More recently, cloud inhomogeneities have complicated understanding of the anomalous shortwave absorption issue [Cess *et al.*, 1995; Imre *et al.*, 1996; Barker, in press, 1998]. A long history of solar radiative transfer modeling of finite clouds indicates the large biases possible with the plane-parallel assumption [e.g., McKee and Cox, 1974; Welch and Wielicki, 1984; Kobayashi, 1993]. But only recently have more realistic cloud descriptions been available for radiative transfer simulations, through improved instrumentation such as ground-based microwave radiometers and millimeter-wave radars.

Although the problem of cloud inhomogeneity in remote sensing is recognized [Rossow, 1989; Chambers *et al.*, 1997], plane-parallel radiative transfer modeling is still the standard approach for cloud property inversions. The neglected processes of horizontal photon transfer and cloud side illumination and shadowing can cause huge errors in cloud optical depth at the pixel scale. In addition, the relationship between cloud characteristics and the satellite pixel size will influence the retrieval [Wielicki and Parker, 1992].

One response to the need for an improved radiative representation of clouds is the independent pixel approximation (IPA) [Cahalan *et al.*, 1994a], a computationally efficient and conceptually simple approach. With this approximation a cloud is subdivided into columns, plane-parallel radiative transfer is applied to each column, and the overall radiative effect is the summation of the contributions from the individual columns. The approximation does not allow for horizontal photon transport between the columns. Using observational data on liquid water path, the IPA seems to capture the domain-averaged radiative properties of marine stratocumulus clouds [Cahalan *et al.*, 1994b].

Copyright 1998 by the American Geophysical Union.

Paper number 98JD00080.  
0148-0227/98/98JD-00080\$09.00

The IPA albedo estimate is close to that predicted by using Monte Carlo methods for bounded cascade cloud models [Cahalan *et al.*, 1994b] and for Landsat-derived models [Barker, 1996b]. By assuming something about the underlying optical depth distribution, such as a gamma distribution, the IPA concept can be extended to general circulation model parameterizations [Barker, 1996a].

The “independent pixel” concept will not improve the remote sensing of cloud properties, as plane-parallel radiative transfer is still being applied to each pixel. Marshak *et al.* [1995] introduced an improvement to IPA that accounts for radiative smoothing, or the tendency of horizontal photon transport to smooth the radiance field that would be expected from applying plane-parallel radiative transfer to the independent columns. The nonlocal independent pixel approximation (NIPA) [Marshak *et al.*, 1998] smooths the outgoing IPA radiance field by convolution with a radiative smoothing kernel.

Most validations of the IPA have relied on thin flat-topped cloud layers containing no vertical variability. In fact, the success of the IPA for domain-averaged quantities has not been demonstrated on clouds containing vertical variations, either internal or at cloud top. The demonstration of NIPA’s value has also assumed vertically uniform clouds. Recently, the radiative effects of cloud top geometry have been used to explain the observed angular dependence of solar radiation from stratocumulus [Loeb *et al.*, in press, 1998].

The potential of IPA and NIPA to increase our understanding of boundary layer clouds requires that the approximations themselves also be well understood. In this study we examine the behavior of 2-D solar radiative transfer in marine stratocumulus clouds and further explore the validity of the independent pixel approximation. The independent pixel approximation is most appropriate for these types of clouds, as they possess a high cloud fraction and are relatively geometrically thick. The data were gathered by a cloud radar during the Atlantic Stratocumulus Transition Experiment (ASTEX). A major strength of the cloud radar is its vertical resolution of 37.5 m. Domain-averaged fluxes are simulated with a forward Monte Carlo model, while upwelling radiances are computed with the spherical harmonics discrete ordinate method (SHDOM). The upwelling reflectances are analyzed to investigate how their spatial variability is affected by cloud structure, particularly cloud top geometry.

We address the following questions:

1. How well does the independent pixel approximation work for domain-averaged fluxes in marine stratocumulus when vertical variations are included?
2. How important are vertical and horizontal variations, both internal to the cloud and at cloud top, to domain-averaged albedos and the spatial variability of cloud top reflectances? Can the spatial variability of reflectances be well described by radiative smoothing, or are other radiative processes important?

3. When realistic cloud top geometry is included, how well does the NIPA method work for calculating radiances? How might it be generalized?

4. How are the errors in remotely sensed optical depth related to measures of cloud inhomogeneity, and what are the implications for the inferred albedo?

The paper is organized as follows. Section 2 describes the cloud radar data set and its conversion into a field of volume extinction coefficients. Section 3 describes the radiative transfer models. The modeling procedures and results are described in sections 4 to 7, while section 8 contains the discussion and conclusions.

## 2. ASTEX Data

ASTEX [see Albrecht *et al.*, 1995] was held in the North Atlantic during June 1–29, 1992. The ostensible purpose of the cloud radar was to document the boundary layer evolution, assist in a large-scale description of the winds, temperature, and moisture fields, and help detail cloud structure. The 35-GHz Doppler radar ( $\lambda=8.66$  mm) was situated on the island of Porto Santo ( $\sim 33^\circ\text{N}$ ,  $16^\circ\text{W}$ ) in the Madeira Islands, off the coast of Morocco. The radar site was on the upwind side of the island, about 100 m from a cliff edge, minimizing any island effect (diurnal variations were similar to those observed from ships [Albrecht *et al.*, 1995]).

### 2.1. Cloud Radar

The radar measures reflectivities and particle velocities and is described fully by Kropfli *et al.* [1995]. The short wavelength and high sensitivity allow for detection of volume extinction coefficients as low as  $4\text{ km}^{-1}$  (for a 40 dBZ echo and cloud droplet number concentration of  $30\text{ cm}^{-3}$ ). A major strength of the radar is its vertical resolution of 37.5 m. The cloud radar operated in a fixed vertically pointing mode for 23 min of each half hour. We rely exclusively on the data gathered while the radar was pointed vertically, with a profile taken every 3 s.

### 2.2. Microwave Radiometer

Independent liquid water path values contribute to the derivation of the cloud optical properties. These were supplied by a National Oceanic and Atmospheric Administration surface-based microwave radiometer located near the cloud radar. The instrument measures the natural microwave emission at three frequencies (20.6, 31.65, and 90 GHz) along its (upwardly pointing) antenna beam. From the microwave emission the total integrated liquid water content can be retrieved by using the statistical technique of Hogg *et al.* [1983], with an estimated uncertainty of 20%. The data were averaged over 30 s.

### 2.3. Conversion to Optical Properties

Radar reflectivities are converted into volume extinction coefficients by using the technique of Frisch *et al.*

[1995]. First, 30-s mean cloud thicknesses are inferred from the “cloudy” radar pixels. Vertically averaged 30-s mean liquid water contents are calculated by dividing the microwave-derived liquid water paths by the 30-s mean cloud thicknesses. From these a cloud-case-mean liquid water content  $q_l$  is found. This is combined with the mean radar reflectivity  $Z$  to calculate a mean cloud droplet number  $N$  from

$$N = 11.11 \rho_w^{-2} q_l^2 Z^{-1} \quad (1)$$

where  $\rho_w$  is the density of water [from *Frisch et al.*, 1995, equation (18)] Once  $N$  is known, a volume extinction coefficient  $\beta$  (referred to here as extinction) for each pixel is calculated according to

$$\beta = 0.9623 Z^{1/3} N^{2/3} \quad (2)$$

The factor 0.9623 includes the geometrical optics limit assumption (extinction equal to twice the integrated droplet cross-sectional area) and parameters of the Frisch et al. lognormal cloud droplet model distribution.

Equation (2) is not valid for drizzling cases, as even a small amount of drizzle will completely dominate the radar signal. Drizzle is common within marine stratocumulus clouds, and some method must be used with which to infer the cloud water field. We adopt a simple nonphysical approach here, as the relationship between cloud water and drizzle is poorly understood [e.g., *Austin et al.*, 1995]. First, nondrizzling cases are preferentially selected: eight of the nine cloud cases contain no inferred drizzle. In the June 8, 2000 case, drizzle is inferred by radar reflectivity values greater than or equal to  $-5$  dBZ and particle fall speeds greater than  $0.97 \text{ ms}^{-1}$ . For these pixels, cloud extinction values are interpolated from the nearby non-precipitating pixels. The extent of drizzle contamination is not entirely known, but its influence should be minor at cloud top, which is most important for the results in this paper.

A horizontal pixel size can be estimated from the mean speed at which a cloud is advected over the radar. A 404-MHz wind profiler was sited at Porto Santo, with

a vertical resolution of 300 m and temporal resolution of roughly 12 min. During all the cases the winds over Porto Santo were weak north-northeasterlies, despite differing synoptics. The mean surface wind speeds varied from 2 to  $6 \text{ ms}^{-1}$ , and the vertical wind shears range from 2 to  $5 (\text{ms}^{-1})\text{km}^{-1}$ . The mean speed taken over all the cases is  $5 \text{ ms}^{-1}$ . We apply this as a reference speed to all nine cases. The increased generality eases intercomparison between the radiance fields with little further loss in accuracy, as wind shear and time averaging already degrade the horizontal pixel size estimate. The resulting 2-D extinction fields are 6.9 km horizontally by 1.1 to 2.1 km vertically, with a 15-m horizontal spacing and an 18.75-m vertical spacing.

Several limitations to our methodology exist. First, the radar-derived clouds and subsequent radiative transfer are two-dimensional, rather than three-dimensional. In a three-dimensional cloud, horizontal radiative transport is more significant than that within a two-dimensional cloud [*Chambers*, 1997] and could lead to a more pronounced difference from the IPA result. Second, the use of an advection speed to convert the radar time series to a spatial field does not necessarily capture the true cloud structure. Last, several assumptions are used to convert radar reflectivity to extinction, such as the fixed droplet concentration and the single-mode lognormal droplet distribution. These assumptions could diminish some of the horizontal and vertical cloud variability, leading to a low bias in the resulting radiative effects.

#### 2.4. Description of Selected Cases

We chose cloud cases with macrophysical cloud variability and a variety of cloud thicknesses. Table 1 lists characteristics for each of the nine cases.

All nine cases have a cloud fraction of one. With these overcast stratocumulus clouds we examine the radiative effects associated with horizontal and vertical variations in extinction values and with cloud top topography. We find that the latter is particularly impor-

**Table 1.** Characteristics of the Nine Cloud Cases

Cloud Case	Mean $\tau$	Mean Ext $\text{km}^{-1}$	Mean $h$ $\text{km}$	std dev $\log_{10}(\tau)$	$\frac{\langle h \rangle}{\sqrt{(1-g)(\tau)}}$ $\text{km}$	Comments
1 June 8 2000	$35.0 \pm 16.1$	$19.0 \pm 12.9$	1.84	0.19	0.80	two internal cloud openings largest cloud top topography
2 June 17 0800	$14.3 \pm 6.5$	$16.4 \pm 9.6$	0.87	0.19	0.60	one interstitial cloud opening
3 June 17 0830	$10.7 \pm 7.2$	$19.2 \pm 12.1$	0.56	0.28	0.44	flat, thin cloud
4 June 17 0900	$6.2 \pm 3.9$	$14.1 \pm 8.4$	0.44	0.29	0.46	two layers of flat, thin cloud
5 June 17 0930	$13.4 \pm 3.7$	$17.7 \pm 11.6$	0.76	0.12	0.54	one fairly uniform layer
6 June 17 1000	$8.3 \pm 1.9$	$11.0 \pm 7.9$	0.75	0.10	0.67	one flat-topped uniform layer
7 June 17 1030	$16.0 \pm 4.3$	$21.6 \pm 11.9$	0.74	0.12	0.48	flat top layer with cloud underneath in parts
8 June 17 1500	$18.3 \pm 3.7$	$18.6 \pm 8.1$	0.98	0.09	0.59	most homogeneous case
9 June 24 1500	$18.4 \pm 4.8$	$14.6 \pm 8.5$	1.26	0.12	0.76	one layer thickening with time significant cloud top bumps

tant to variability in the upwelling reflectances and that the cases divide themselves naturally into two groups on the basis of their cloud top structure. Two of the cases have significant cloud top topography, with cloud top variations (the difference between a local height maximum and a nearby minimum) reaching 200 m. These are the June 8, 2000 (depicted in Figure 1) and June 24, 1500 (Figure 2c) cases. For these two cases the cloud

top bumps tend to be associated with higher extinction values. Perhaps not coincidentally, these two cases are also the thickest clouds, both optically and geometrically. The other seven cases have much more even cloud tops, with cloud height variations of mostly 40 m and occasionally 75 m, as shown in the examples of Figures 2a and 2b. For these cases the cloud top bumps do not necessarily contain higher extinction values.

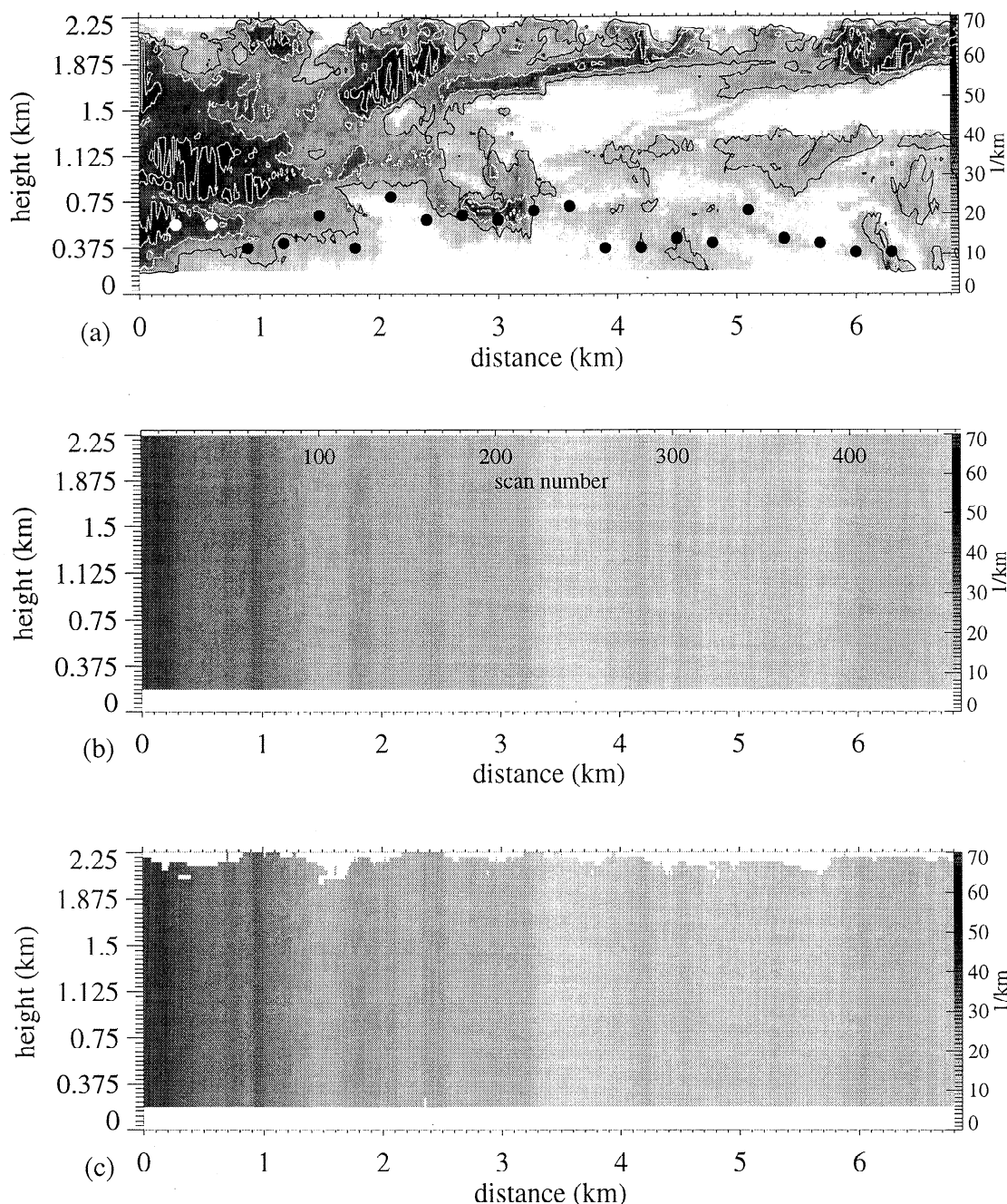


**Figure 1.** (a) Volume extinction coefficients for the June 8, 2000 case. White and black dots denote the ceilometer-derived cloud base height. The ceilometer has 15-m vertical resolution and 1-min temporal resolution. Black, white, and white contour levels indicate extinctions of 15, 30, and 45  $\text{km}^{-1}$ , respectively. (b) The same cloud represented using the uniform pixel approximation (UPA), (c) The same case with the uniform pixel approximation and the original cloud top topography (bump).

To elucidate the underlying causes of variability in the radiative fields, we construct three versions of the same cloud field, illustrated for one example in Figure 1. Figure 1a shows the extinction field of the two-dimensional cloud. Figure 1b has the same optical depth structure as that in Figure 1a, but now the optical depth is distributed evenly throughout the column. The cloud top and base are flat and horizontally even and correspond to the maximum cloud top height and minimum cloud base height existing within

Figure 1a. We call this version the uniform pixel approximation (UPA). This cloud field is similar to the cloud field constructed by *Cahalan et al.* [1994a] from vertically integrated liquid water content data to develop and justify the IPA. Figure 1c is a variation on the UPA, in which each column has one vertical mean extinction value, but the original cloud top topography is kept. This is called the bump approximation and helps articulate the contribution of the cloud top geometry to the radiance field. All three versions possess an

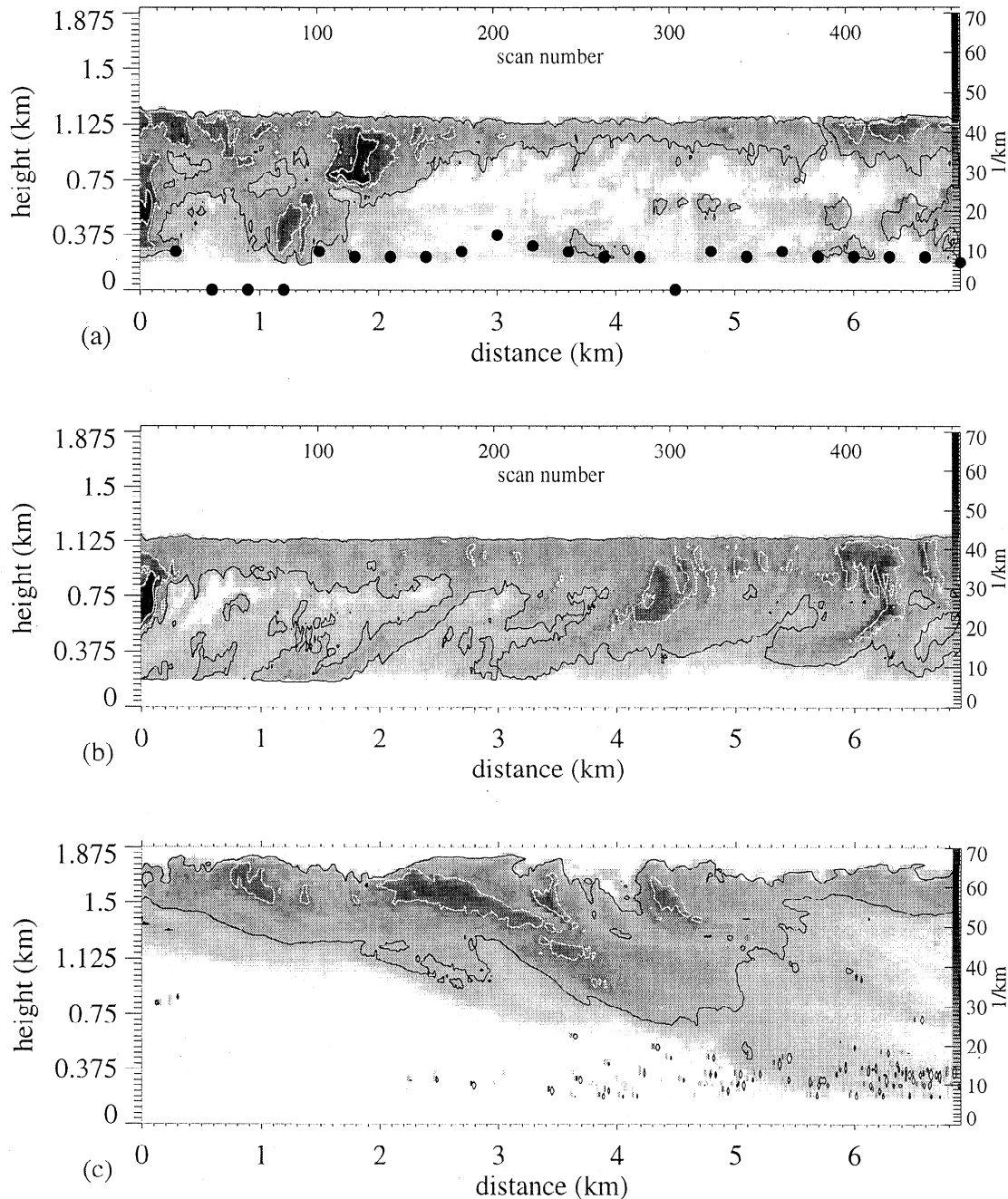


**Figure 2.** Volume extinction coefficients for three cloud cases: (a) the June 17, 800 case, including ceilometer cloud base heights shown as black dots, (b) the June 17, 1500, and (c) the June 24, 1500 case. Black, white, and white contour levels indicate extinctions of 15, 30, and 45  $\text{km}^{-1}$ , respectively.

identical optical depth field, and the IPA will yield the same radiative fields for all three cloud descriptions.

Cloud base height can be difficult to obtain from radar. The lowest five range gates contain ground clutter and are excluded; this approach establishes an artificial cloud base height of 187 m for all of the cases. Other determinations of cloud base height, done with a ceilometer or through a more stringent method [Uttal and Frisch, 1994], place cloud bases close to or above 190 m. Although our cloud bases are probably too low, an accurate determination of cloud base is not important to this work. The extinction values near cloud base are small, and thus their radiative contribution is small. In contrast, details about the cloud top are radiatively important and well articulated by the radar.

Figure 2 contains three more examples of the cloud radar cases. Figure 2a shows the June 17, 800 case. Of the seven cases that lack significant cloud top topography, the June 17, 800 case shown in Figure 2a is perhaps the most internally inhomogeneous. Figure 2b shows the June 17, 1500 case. It is the most homogeneous of the nine cases and optically and geometrically thicker than most. This case will be used throughout the paper to exemplify the seven more homogeneous cases. Figure 2c shows the June 24, 1500 case, which is the other case besides the June 8, 2000 case with significant cloud top height variation.

### 3. Models

#### 3.1. Spherical Harmonics Discrete Ordinates Method

The primary radiative transfer model used is the spherical harmonics discrete ordinates method (SHDOM) [Evans, 1998]. This model represents the radiation field explicitly, and can efficiently compute many outgoing radiances. It represents the angular part of the source function with a spherical harmonic series and the spatial part with a discrete grid. The radiative transfer solution is arrived at by iterating between the source function and the radiance field as follows: (1) the source function is transformed from spherical harmonics to discrete ordinates, (2) the integral form of the radiative transfer equation is used to obtain the radiance along the discrete ordinates, (3) the radiance is transformed back to spherical harmonics, and (4) the source function, including the scattering integral, is computed from the radiance field. The advantage of this procedure is that it can attain an accurate solution efficiently, in terms of both time and memory usage. Memory is saved by using an adaptive length to the spherical harmonic series for each grid point and by using an adaptive grid, in which grid points are added only where needed. The model can also be run in an independent pixel mode, where the input columns do not interact horizontally.

The model has much freedom in setting model parameters, which determine the trade-off between computer

resources and output accuracy. Here the domain size is 460 horizontal grid points by 60 to 112 vertical grid points, depending on the cloud thickness. The SHDOM internal grid resolution is 15 m horizontally and 18.75 m vertically. The cell-splitting accuracy for the adaptive grid is set to 0.01 (for an incident solar flux of unity). The angular resolution is determined by 16 discrete ordinate zenith angles and 32 azimuth angles.

The extinction is specified at each grid point, but the other optical properties are held fixed. Conservative scattering is assumed. A phase function for 0.83- $\mu\text{m}$ -wavelength light interacting with a distribution of droplets having an effective radius of 10  $\mu\text{m}$  is used. The delta-M method and the TMS method of Nakajima and Tanaka [1988] give good accuracy for radiances from the highly peaked phase function. The surface albedo is set to zero. We use open boundary conditions horizontally, in which no reflection occurs from the boundaries and the radiation incident on the sides is from plane-parallel transfer using the domain end columns. An open boundary condition precludes radiative effects caused by large edge gradients in optical depth. The output variables used here are the upwelling radiance from the top at every grid point.

Two solar zenith angles ( $0^\circ$  and  $60^\circ$ ) are run for each different cloud representation, at an azimuth angle of  $0^\circ$ . Because of the very high density grid the CPU time required on an HP 715/75 ranges from 30 to 60 min, depending on cloud thickness, Sun angle, and cloud field representation. Radiance error is expected to be about 1% based on previous testing [Evans, 1998, Table 4]. Total flux, including the flux leaving the domain sides, is conserved to within 1%.

#### 3.2. Monte Carlo

Monte Carlo radiative transfer is more efficient than SHDOM at computing accurate domain-averaged fluxes. The forward Monte Carlo model implemented uses the maximal cross section method described by Marshak *et al.* [1995]. It reads the same medium input files as SHDOM and outputs domain-averaged flux, pixel level fluxes, and Green's function spot sizes. Periodic horizontal boundary conditions are assumed. Comparisons with the Marshak *et al.* [1995] model give agreement to within the expected Monte Carlo noise. For the runs shown here,  $10^6$  photons are used. The rms Monte Carlo noise in domain-averaged albedo is 0.001. The Monte Carlo model is applied to double-wide periodic domains made by appending the mirror image of the extinction field. Such a construction avoids generating artificial gradients in the optical depth.

### 4. Domain-Averaged Radiative Transfer

Previous studies [Cahalan *et al.*, 1994b; Barker, 1996b] have concluded that the independent pixel approximation is capable of capturing the domain-averaged albedo

**Table 2.** Domain-Averaged Albedos for the Nine Cloud Cases

Case	SZA= 0°			SZA= 60°		
	2-D	$\Delta$ IPA	$\Delta$ PPA	2-D	$\Delta$ IPA	$\Delta$ PPA
June 8 2000	0.697	0.006	0.037	0.796	0.002	0.025
June 17 0800	0.474	0.003	0.034	0.642	0.002	0.025
June 17 0830	0.367	0.004	0.053	0.553	0.004	0.053
June 17 0900	0.253	0.001	0.022	0.454	-0.002	0.038
June 17 0930	0.475	0.003	0.015	0.644	0.002	0.011
June 17 1000	0.346	0.000	0.006	0.549	0.001	0.007
June 17 1030	0.518	0.004	0.017	0.673	0.004	0.013
June 24 1500	0.568	0.001	0.007	0.708	0.000	0.006
June 24 1500	0.566	0.001	0.013	0.703	0.003	0.013

Domain-averaged monochromatic albedos for two solar zenith angles for each of the nine clouds, using two-dimensional (2-D) radiative transfer, the independent pixel approximation (IPA), and the plane-parallel approximation (PP).  $\Delta$ IPA and  $\Delta$ PPA correspond to the IPA-2-D and PPA-2-D albedo, respectively.

of a marine stratocumulus field. This is indeed what we find within the nine cloud cases investigated here. Table 2 shows the domain-averaged monochromatic albedo for 2-D radiative transfer and the domain-averaged IPA-2-D and PPA-2-D albedo differences.

Differences between 2-D and plane-parallel albedo range between 1.5% and 15%, with a mean of about 5%. The difference between the IPA and plane-parallel albedo is smaller than that found by *Cahalan et al.* [1994b] and by *Cahalan and Silberstein* [1995] using ASTEX liquid water path data under overcast conditions. This difference occurs probably because our domain contains a smaller range in optical depth than the microwave liquid water path data, which were gathered throughout 8 days of ASTEX. The independent pixel approximation works very well, with a difference from 2-D that is always less than 1.0%. No dependence on Sun angle is seen. The bias is nearly always positive (i.e.,  $\text{IPA} > \text{2-D}$ ), indicating that overall horizontal photon transport must also be increasing the downward photon flow. This result must be a consequence of vertical inhomogeneities either internal or at cloud top, as, in contrast, the IPA albedos are lower than the UPA albedos by up to 0.005 under an oblique Sun (not shown), consistent with Figure 6 of *Cahalan et al.* [1994b] and Figure 5 of *Barker* [1996b]. The 2-D albedo calculated using SHDOM (not shown) agrees to within 0.01 of the Monte Carlo calculated albedo, increasing our confidence in the SHDOM results.

## 5. Spatial Variability of Reflectance Fields

### 5.1. Nadir Reflectance Fields

For remote sensing purposes the reflectance fields are more important. We examine the reflectances at nadir, which is the viewing angle of the Landsat satellite, for

solar zenith angles of 0° and 60°. The reflectance field at the original horizontal resolution (15 m) is close to the Landsat pixel-size resolution (28.75 m). By averaging the reflectances over larger scales we emulate remote sensing by satellites with larger pixel sizes, such as the Advanced Very High Resolution Radiometer. Two examples are shown to illustrate the radiative effects of the four approximations, after which we quantify the variability using power spectra.

The nadir reflectances for the most homogeneous case, that of June 17, 1500, illustrates a “best agreement” case (Figure 3). The 2-D, UPA, and bump reflectance fields roughly agree for the overhead Sun case. All three are smoother than the IPA reflectance field. The main disagreement for both Sun angles occurs within the first kilometer of the cloud, where vertical and horizontal inhomogeneities are the most marked. At a low Sun angle the relationship between the 2-D, UPA, bump and IPA reflectances is less consistent. Differences between the oblique Sun angle reflectance fields are usually small, at about 5%. The differences reach 15% only in places with strong vertical inhomogeneity, both internal, such as within the first cloud kilometer, or at cloud top, such as at distance 2.5 km. The cloud top topography is minimal, never exceeding one pixel height, but still capable of generating differences between the reflectance fields. The June 17, 800 case, which possesses more internal variability than this 1500 case, consequently also shows more discrepancy between its 2-D and UPA reflectance fields than is evident in the June 17, 1500 reflectances.

Figure 4 shows the nadir reflectances for a case with strong vertical inhomogeneity, that of June 8, 2000. Under an overhead Sun, cloud vertical variations do not have a large radiative effect, as shown by radiatively smoothed 2-D, UPA, and bump reflectances that are usually within about 5% of each other. The 2-D reflectances can be slightly higher or lower than the UPA



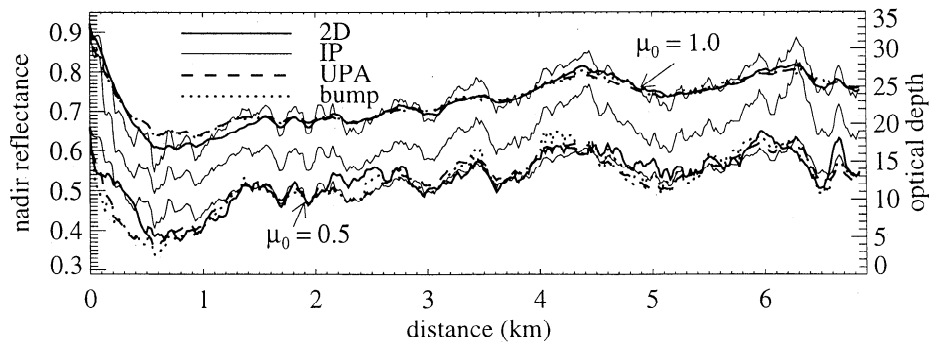


**Figure 3.** Nadir reflectances for the June 17, 1500 case at overhead Sun and a solar zenith angle of  $60^\circ$  and the June 17, 1500 optical depth trace. Reflectance for the fully two-dimensional case is depicted by a thick solid line, reflectance for the independent pixel approximation with a thin solid line, reflectance for the uniform pixel approximation with a dashed line, and reflectance for the UPA plus cloud top topography case is shown by a dotted line. The optical depth trace is shown as a thin solid line lying between the two reflectance sets.

and bump reflectances, depending on the cloud top extinction value. The IPA field shows more extreme variations and can differ from the other three fields by up to 15%.

Much more remarkable are the differences between the reflectance fields at a low Sun angle. Now, the 2-D reflectances are highly variable, more so than the IPA reflectances, and differences between the two can be more than 25%. The UPA reflectance structure is the smoothest, and the addition of cloud top geometry to the UPA field clearly improves agreement to the 2-D field by capturing bump side brightening/shadowing

effects. The ordering of the extreme values of the 2-D, UPA, and bump reflectances must be caused by the high extinction values contained within the 2-D cloud bumps. The June 24, 1500 case is very similar. It also has strong variability in the low-Sun-angle 2-D field and has cloud bumps and pockets coinciding with high/low extinctions.

## 5.2. Power Spectra

Power spectra for the above cases help quantify the differing amounts of variability. Spectra for the June 17, 1500 and June 8, 2000 cloud cases and for the mean

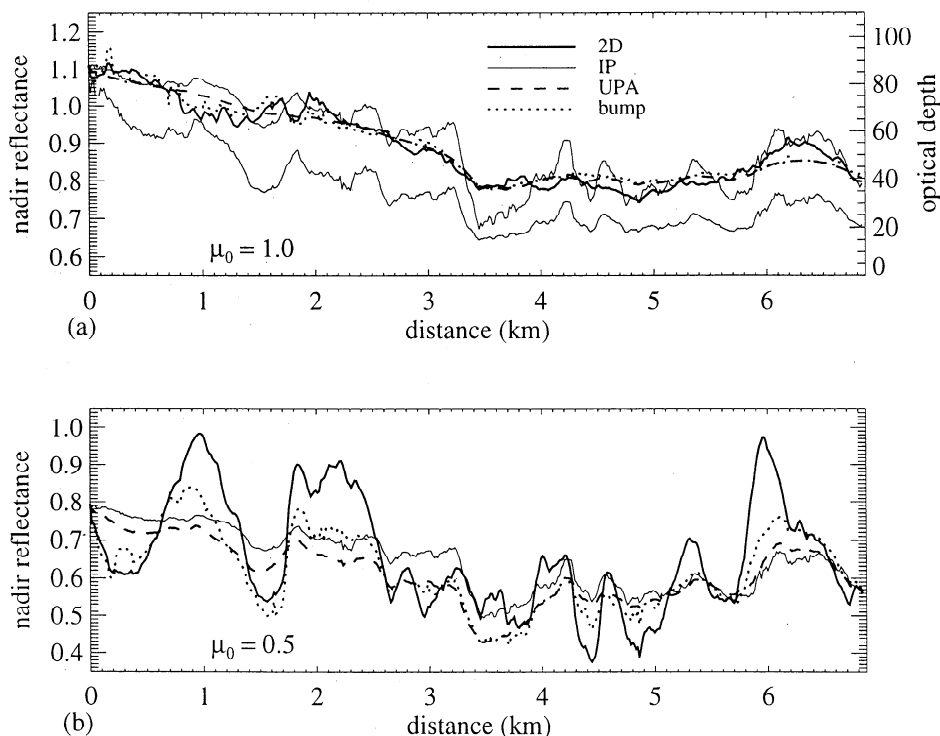


**Figure 4.** Similar to Figure 3 but for the June 8, 2000 case, at (a) overhead Sun, which includes the optical depth trace, and (b) a solar zenith angle of  $60^\circ$ . Line style conventions are the same as those in Figure 3.



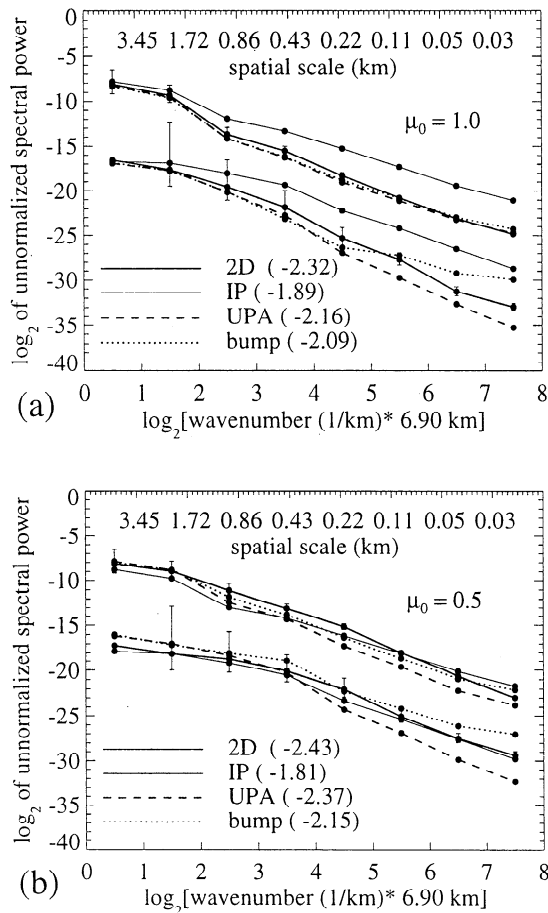


**Figure 5.** Power spectra for the June 17, 1500 case and mean power spectra for all nine cloud cases at (a) overhead Sun and (b) a solar zenith angle of 60°. The nine-cloud-case-mean spectra are displayed with a vertical offset of +5. Linestyle conventions are the same as those in Figures 3. The 95% confidence intervals are shown as error bars on the spectra. Nine-cloud-case-mean power spectrum bestfit slopes between wavenumbers 2.5 and 7.5 are given in parentheses for each of the four approximations.

of all nine cloud cases are shown, illustrating the full range of cloud top inhomogeneity. The mean and trend are removed from the original reflectances before producing the spectra shown in Figures 5 and 6. The spectra are averaged into octave-wide wavenumber bins and are shown on a  $\log_2$ - $\log_2$  plot. The slope of the power spectra for wavelengths below about 1 km is indicated.

Figure 5 shows the unnormalized power spectra for the June 17, 1500 cloud case at the two Sun angles for the 2-D, UPA, bump, and IPA reflectance field. The spectra for the nine cloud case mean are also shown and include a vertical offset of 5. As seen in Figure 5, the June 17, 1500 and cloud-case-mean power spectra for all four radiative approximations are about the same at the largest spatial scales. For both sets of spectra and under an overhead Sun, the UPA, bump, and 2-D spectra begin to fall away from the IPA spectrum at 1–2 km. This behavior indicates that the radiative smoothing scale has a wavelength  $L$  of 1–2 km, or a wavenum-

ber  $k \approx 1/200$  m, demonstrating the spatial extent of radiative smoothing. This finding is true for all of the homogeneous cases. At the smaller spatial scales, the 2-D, UPA, and bump spectra are fairly similar for the nine-cloud-case mean, as they are for most of homogeneous cloud cases. For the June 17, 1500 case, however, at the smaller spatial scales, the bump reflectances contain more power than the 2-D radiances, and the UPA reflectances have the least power. The reasons for this difference are not completely clear. For both sets of spectra and under an oblique Sun the spectra for all four radiative approximations lie much closer to each other. This finding reflects the enhanced interaction of the cloud top geometry with the Sunlight and masks any signal associated with radiative smoothing. The increase in variability is particularly noticeable at the smaller spatial scales.

Figure 6 shows the power spectra for the vertically inhomogeneous June 8, 2000 case. The higher degree of intrinsic variability for this cloud in relation to the June 17, 1500 case is reflected in the increased spectral power at large spatial scales. The most interesting aspect of the spectra occurs for an oblique Sun angle. As seen in Figure 6b (and in contrast with Figure 5b), the 2-D reflectance spectra contain much more variance than the IPA reflectances, particularly at the intermediate

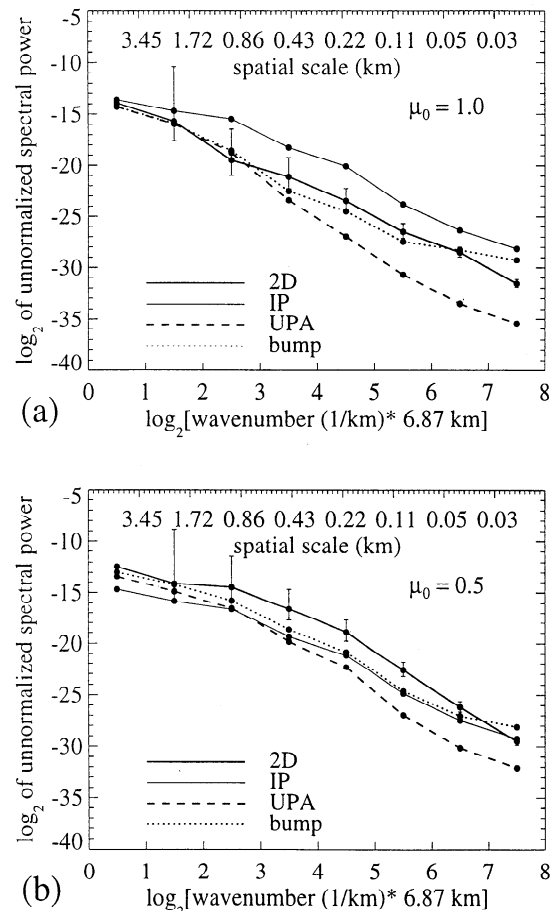


**Figure 6.** Similar to Figure 5 but for June 8, 2000.

spatial scales lying between 50 m and 1.2 km. This behavior reflects the impact of the larger topographical features.

Previous studies have used power spectra slopes to quantify the spatial scale at which radiative smoothing becomes important [e.g., *Davis et al.*, 1997, and references therein]. Such an analysis is of limited use here, given the small data set size. Nevertheless, we have included slope values for the mean spectra of the nine cloud cases, for scales smaller than about 900 m, within Figure 5 for the sake of completeness and for comparison with other studies. The mean IPA small-scale slope of  $-1.9$  is reasonably close to the  $-5/3$  slope expected for turbulence. The 2-D, UPA, and bump spectra for overhead Sun have slightly steeper slopes that reflect a radiative smoothing or diminishing of the smallest-scale variability, but the slopes are not as steep as those seen within Landsat data [*Davis et al.*, 1997]. The overall similarity between the 2-D and UPA spectra implies that, on average, vertical inhomogeneities do not affect the spatial variability much for overhead Sun. For an oblique Sun the slope values are meaningless. Cloud side illumination and shadowing increase the 2-D and UPA spectra power at all the spatial scales, an effect not captured by the slope values. For all nine cases the 2-D variance exceeds or is equal to the IPA variance at all but the very smallest spatial scale, and no radiative smoothing signal is apparent.

## 6. Smoothing Scale and Improved NIPA

A non-statistical procedure more appropriate to this data set is used to determine the smoothing scale. The procedure compares the 2-D and IPA nadir reflectances, using a variation on a technique developed by *Marshak et al.* [1995], called the nonlocal independent pixel approximation (NIPA). This technique approximates 2-D radiative transfer by convolving the IPA reflectances with a smoothing kernel to form a NIPA reflectance field. *Marshak et al.* [1995] determine the smoothing kernel width from diffusion arguments. Here, instead, we use NIPA to estimate the smoothing scale, by finding the width of the smoothing kernel that gives the highest correlation between the NIPA and 2-D reflectances. The smoothing kernel we use is a Gaussian distribution, because its smoothing scale, the standard deviation  $\sigma$ , is the same for one-dimensional and two-dimensional convolution.

The procedure for obtaining the smoothing scale is illustrated in Figure 7, using the June 24, 1500 case as an example. The IPA reflectances are convolved with Gaussians of varying widths, and the correlation of the 2-D and NIPA reflectances is plotted as a function of the smoothing scale  $\sigma$ . The convolution is not valid at the ends of the domain, so that only the center 4 km are used. For overhead Sun the correlation is high and peaks over a broad range of  $\sigma$ . This behavior is typical for all of the cases and indicates that the smoothing scale cannot be defined precisely. For low Sun, the cor-

relation is low and peaks for  $\sigma \approx 0$ . This means that radiative smoothing, while undoubtedly occurring, is completely masked by other effects.

In addition to radiative smoothing, we expect the geometric interaction of the direct solar beam with the cloud top variations to be important. A simplified way to model the direct beam geometric effect is to compute the three-dimensional direct beam flux and use it in the pseudo-source for the independent pixel diffuse radiative transfer. We denote this approximation, which was first developed by *Gabriel and Evans* [1996], by 3dbIPA (for 3-D direct beam IPA) and note that it is an option in SHDOM. The true 3-D direct beam pseudo-source is easily computed for all columns, so this approximation is as efficient as IPA. Figure 8b compares the 3dbIPA and IPA reflectances for the low-Sun June 24, 1500 case. The 3dbIPA reflectance does show more of the desired structure than the IPA, but it has wild fluctuations. This hypersensitivity to small-scale cloud top variability is due to the side illumination and shadowing effects of the 3-D direct beam. The independent pixel diffuse radiative transfer can only move flux vertically, so the 3-D direct beam controls the flux emanating from the column.

A much better approximation is to smooth the 3dbIPA reflectances. This procedure simulates the effects of horizontal diffuse transfer and eliminates the wild fluctuations. We call this approximation 3dbNIPA, as it is essentially the nonlocal independent pixel approximation, except that it starts with the 3dbIPA reflectances. Figure 8b shows that 3dbNIPA reflectances (with the  $\sigma$  having the highest correlation) are reasonably close to the 2-D reflectances. For overhead Sun, as shown in Figure 8a, 3dbNIPA and regular NIPA are equivalent.

The correspondence of reflectances computed with various radiative transfer approximations is summarized with the correlations shown in Figure 9. The

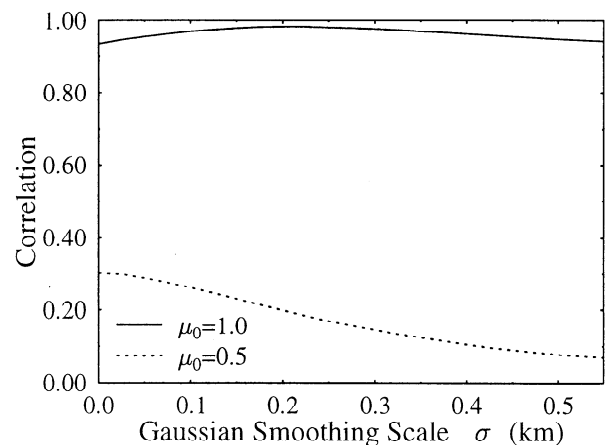


**Figure 7.** Correlation of the NIPA and 2-D reflectances as a function of smoothing scale. The correlation curve is shown for two Sun angles for nadir reflectances from the June 24, 1500 case. The best fit  $\sigma$  is found from the maximum correlation, giving  $\sigma = 0.200$  km for  $\mu_0 = 1$  and  $\sigma = 0.0$  km for  $\mu_0 = 0.5$ .

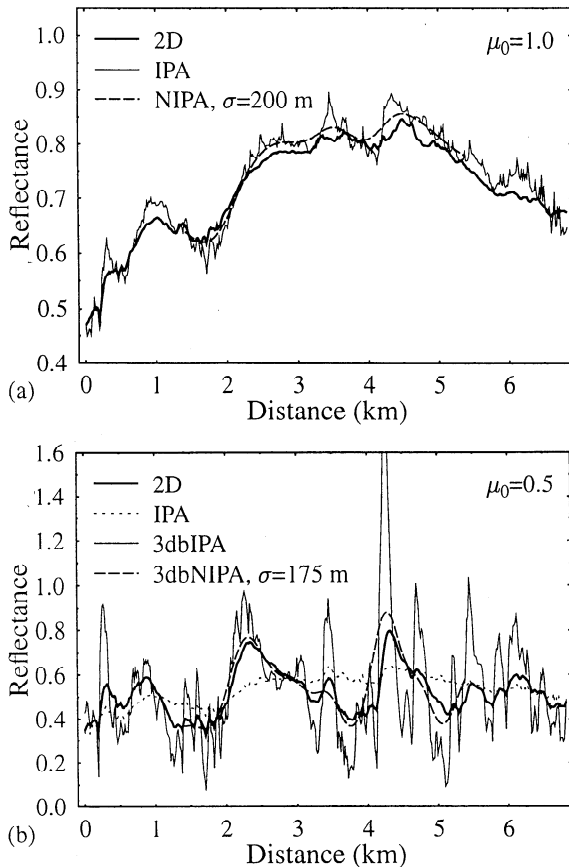


**Figure 8.** Nadir reflectances comparing 2-D radiative transfer results with independent pixel approximation (IPA), nonlocal IPA (NIPA), 3-D direct beam IPA (3dbIPA), and 3-D direct beam nonlocal IPA (3dbNIPA), for (a) overhead Sun and (b) low Sun.

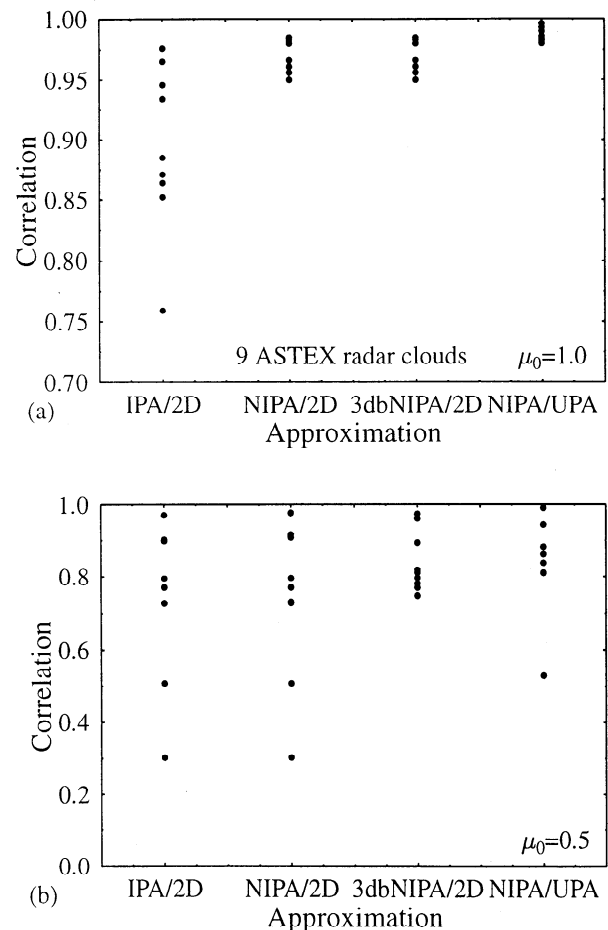
overhead Sun case ( $\mu_0 = 1$ ) shows that while IPA is not that poor an approximation to 2-D, NIPA offers a very substantial improvement, with correlations exceeding 0.95. For low Sun the situation is completely different. The IPA reflectance correlations are much lower, and regular NIPA does not help at all. Even comparing NIPA with 2-D transfer in a vertically uniform medium (UPA) shows some poor correlations. The 3dbNIPA reflectances show much better correlation with the 2-D reflectances than either IPA or regular NIPA.

Figure 10 shows the best fit smoothing scales for the nine cloud cases. For overhead Sun the  $\sigma$  range from 0.025 to 0.450 km for the 2-D medium, but the range for the vertically uniform medium is narrower, ranging from 0.125 to 0.325 km, with a typical scale of 150 m. This finding suggests that even for overhead Sun, vertical variability has some influence in individual cases. The typical NIPA-derived scale  $\sigma$  is consistent with the wavenumber  $\hat{k} = 2\pi/L$  estimate of  $1/200$  m seen within Figures 5 and 6. The Fourier representation of a Gaussian filter contains a “break” at the inflection point  $\hat{k} = 1/\sigma$ . Equating the two estimates, we find  $L = 2\pi\sigma \approx 1.2$  km.

For low Sun the best fitting NIPA  $\sigma$  is usually 0.050 km or less, indicating again a masking of the radiative

smoothing process. In contrast, the 3dbNIPA smoothing scale for  $\mu_0 = 0.5$  ranges from 0.150 to 0.250 km, consistent with the smoothing scale derived for overhead Sun. This finding also demonstrates that a good radiative description can be achieved if both geometrical and radiative smoothing processes are accounted for.

Figure 10 also relates the NIPA-derived smoothing scale to a diffusion-derived smoothing scale  $\eta$ . The diffusive smoothing scale is given by  $\eta \approx \bar{h}/\sqrt{(1-g)\bar{\tau}}$  [Marshak *et al.*, 1995], where  $\bar{\tau}$  is the average optical depth,  $g = 0.85$  is the asymmetry parameter, and  $\bar{h}$  is the mean cloud thickness (here for the central 4 km region with a  $5 \text{ km}^{-1}$  cloud threshold). For overhead Sun there is a barely significant correlation between the best fit Gaussian and the diffusion smoothing scales. Noteworthy is that the diffusive and best fit smoothing scales occupy substantially different ranges: for NIPA/UPA the average is  $\sigma = 0.20$  km, whereas the average  $\eta = 0.55$  km. The Gaussian smooth-



**Figure 9.** Correlation between reflectance curves for several radiative transfer approximations for the nine ASTEX radar-derived cloud fields. IPA or NIPA reflectances are compared with 2-D radiative transfer in either the 2-D medium or the vertically uniform medium (UPA). For the NIPA cases the best fit Gaussian  $\sigma$  is used. Note the different scales for (a) overhead Sun ( $\mu_0 = 1$ ) and for (b) low Sun ( $\mu_0 = 0.5$ ).

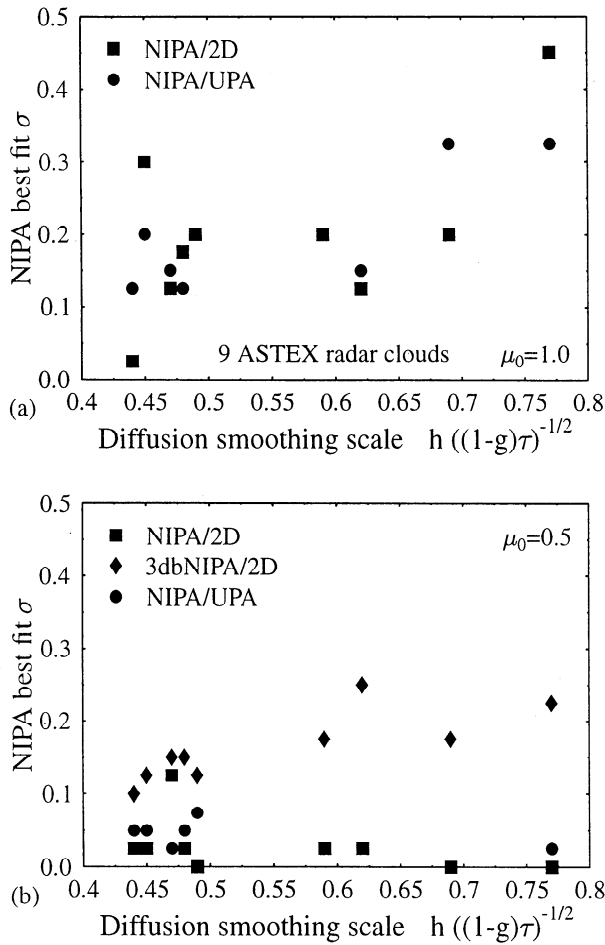


**Figure 10.** Smoothing scale  $\sigma$  estimated from the Gaussian NIPA process as a function of the diffusive scale estimate  $\bar{h}/\sqrt{(1-g)\tau}$  for the nine ASTEX radar-derived cloud fields, for (a) overhead Sun and (b) a solar zenith angle of  $60^\circ$ . The smoothing scale is estimated by comparing Gaussian-convolved IPA reflectances with 2-D reflectances in 2-D and UPA media.

ing width  $\sigma$  is related to the gamma smoothing kernel parameter  $\eta_{\text{Marshak}}$  of Marshak *et al.* [1998] by  $\sigma^2 = \alpha(\alpha + 1)\eta_{\text{Marshak}}^2$ , found by equating the second moments of a gamma and Gaussian distribution with the radius measured from the origin. For the gamma distribution smoothing kernels reported by Davis *et al.* [1997],  $\eta_{\text{Marshak}} \approx 0.6\sigma = 0.6 * 0.2 = 0.12$  km, which is only about one fourth the diffusion smoothing scale  $\bar{h}/\sqrt{(1-g)\tau}$ . The discrepancy between the empirically derived and diffusion-derived smoothing scale may reflect an oversimplified view of the diffusion process that ignores the presence of vertical inhomogeneities and low optical depth regions within the cloud cases.

## 7. Application to Remote Sensing of Optical Depth and Albedo

Remote sensing methodologies typically retrieve optical depth and estimate the true albedo by applying plane-parallel theory to observed reflectances. We can judge the efficacy of such remote sensing retrievals, at a

variety of spatial scales, by using the following methodology on the nadir reflectances.

1. Average the “observed” 2-D and IPA reflectances over a particular spatial scale. The spatial scales are chosen to reflect fractions of the original domain; for example, at a spatial scale of 3.4 km the original domain is halved, and calculations are made separately for each half of the original domain.

2. “Retrieve” the corresponding optical depth and albedo from a lookup table made by using plane-parallel theory. The retrieved optical depth is not allowed to exceed a value of 100.

3. Compute the domain-averaged difference between the “retrieved” and the true optical depth or albedo.

Figure 11 shows the difference between the reflectance-retrieved optical depths and the “true” optical depths for the two Sun angles as a function of spatial scale. In

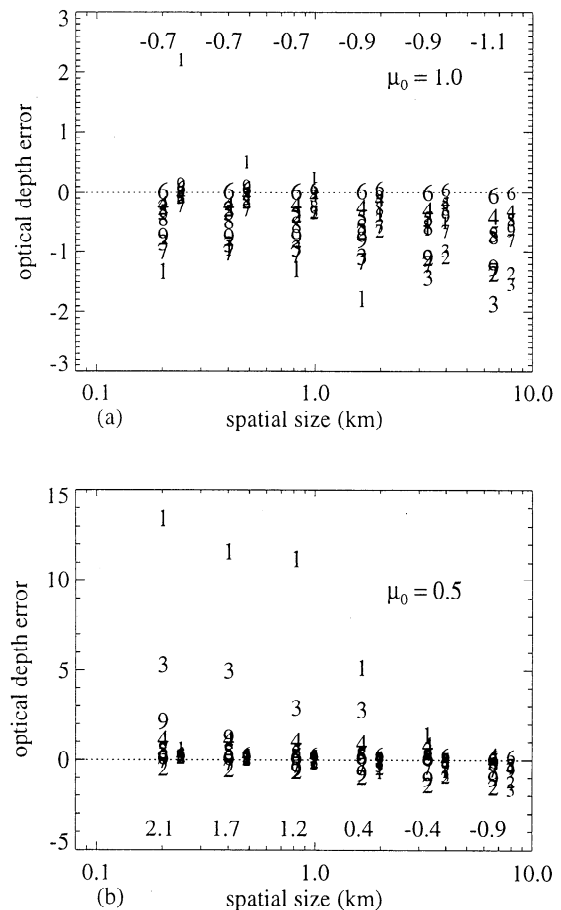


**Figure 11.** Difference between the reflectance-derived and true optical depth for all nine cloud cases as a function of spatial scale for (a) overhead Sun and (b) a solar zenith angle of  $60^\circ$ . The domain-mean difference for each cloud case is indicated by its numerical label from Table 1. Optical depths are derived from both the 2-D and IP reflectances. The 2-D optical depth error is shown in a larger font than the IP optical depth error and is located at the appropriate spatial scale. The IP optical depth error is located to the right of the 2-D optical depth error. The mean 2-D differences over the nine cloud cases are listed.

practice, spatial subsets containing true optical depths exceeding 60 are excluded, as small differences between the reflectance calculations done at large optical depths for the lookup table and the cloud cases translate into large artificial optical depth differences. Differences are shown for both 2-D and IP optical depth errors.

The IP optical depth error reflects the sole influence of horizontal variability in optical depth. It is a negative bias, reflecting Jensen's inequality that, given a convex reflectance optical depth relationship, the mean reflectance is less than the reflectance of the mean optical depth. As Figure 11 shows, this negative "IP bias" increases with spatial scale as the optical depth distribution becomes wider, a result also seen by *Davis et al.* [1997]. The bias is generally larger for the more variable clouds. The slight positive bias that exists at the smaller spatial scales is caused by slight differences between the SHDOM reflectance values for the lookup table and those for the cloud cases with large optical depth sections, such as for cloud case 1.

A comparison of the 2-D optical depth error with the IP optical error provides an estimate of the influence of horizontal transport. With an overhead Sun the mean 2-D reflectance-derived optical depths are usually less than the IP optical depths at all scales. This finding suggests that the presence of horizontal transfer decreases the cloud top reflectance. The mean difference for all the clouds increases slightly with increasing spatial scale, primarily reflecting the increased width of the underlying optical depth distribution. At the largest scale the optical depth error of 1.1 is a small but significant error, given an average optical depth of 15.6. At small scales the rms optical depth error for the individual domain subsets is large as a result of local 2-D effects (not shown), but the bias is small.

Under low Sun the 2-D optical depth error is much more variable. It remains negative at the large spatial scales but can become large and positive at the small spatial scales. At the small scales the range of 2-D reflectance is expanded for the cases with significant cloud top topography, leading to a higher retrieved optical depth. This is the opposite effect of what occurs at large scales, where averaging narrows the reflectance range and the negative IP bias dominates. For the June 8, 2000 case the expanded range of reflectances at small scales produces a mean optical depth error of 13, or about onethird the average optical depth. These results are consistent with a comparison by *Loeb and J. A. Coakley* [in press, 1998] of AVHRR reflectances and plane-parallel theory for marine stratocumulus. In a Monte Carlo modeling study, *Loeb and Varnai* [1997] also find 3-D nadir reflectances for overcast clouds that are reduced under overhead Sun and increased under low Sun, which they attribute primarily to cloud top structure.

The dependence of the optical depth retrieval on the mean optical depth  $\bar{\tau}$ , the standard deviation of the optical depth  $\sigma_{\tau}$ , and the gamma parameter  $(\bar{\tau}/\sigma_{\tau})^2$  used

by *Barker* [1996a] is investigated. Each of these parameters can be physically expected to correlate with the retrieved optical depth, and both *Barker* [1996a] and *Chambers et al.* [1997] find the best correlation to occur with the gamma parameter. With this sample and at both Sun angles we find little correlation at the small spatial scales and some correlation at the large spatial scales. At the larger spatial scales, horizontal variations in optical depth are more influential, consistent with Figure 11, while the lack of correlation at small spatial scales may reflect the unaccounted-for influence of cloud top geometry upon the retrieval. Even less correlation is seen between the albedo error and each of these three parameters.

A further aspect of the dependence of the retrieval on cloud top geometry and spatial scale is demonstrated in Figure 12, which shows the difference between the retrieved and true optical depth as a function of the difference between the maximum and minimum cloud top height existing within the spatial scales of 1.70 km and 210 m, for a Sun angle of 60°. Retrieval errors

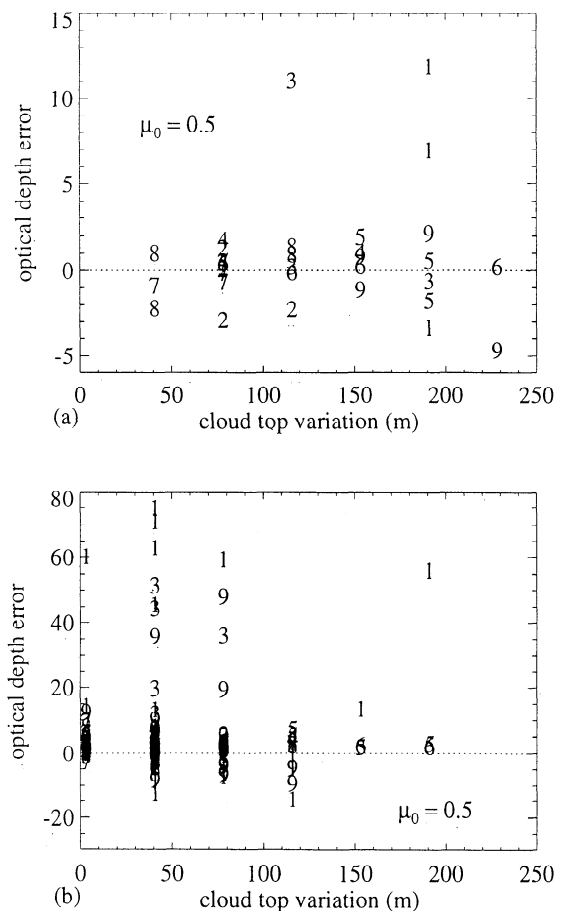


**Figure 12.** Difference between the reflectance-derived and true optical depth for all clouds at a solar zenith angle of 60° as a function of the maximum cloud top height variation, shown for a spatial scale of (a) 1.70 km, and (b) 210 m. Differences are shown for all individual domain subsets. Each cloud case is indicated by its numerical label from Table 1.

are shown for each of the individual domain subsets. The interesting aspect of this figure is that it is not the maximum cloud top height variation that has the strongest influence on the error, but rather, the ratio between the maximum cloud top variation and the horizontal spatial scale. At a spatial scale of 1.7 km the largest retrieval errors occur for the domain subsets containing 3-5 pixel (112-187 m) bumps. At the smallest spatial scale of 210 m, most of the large retrieval errors occur for the domain subsets containing one-pixel-height (37.5 m) bumps. The retrieval errors can be substantially larger at the smaller spatial scale, indicating again the increased importance of cloud top geometry at smaller scales. The same pattern of the retrieval error on cloud top geometry and spatial scale occurs under overhead Sun, although the retrieval errors overall are smaller. The remote sensing implication is that the difficulty of retrieving optical depths accurately for different cloud types varies with satellite pixel size.

A related question that has also been addressed by *Chambers and Wielicki* [1997] is, how well does plane-parallel theory apply to the remote sensing of albedo? Assuming the validity of the independent pixel approximation for larger areas, the albedo error depends on the error in the distribution of optical depth within a particular area and not on the pixel-by-pixel errors. This issue is addressed similarly to the optical depth retrieval error analysis.

Figure 13 shows the difference between the 2-D reflectance-derived albedo and the “true” albedo as a function of spatial scale. For overhead Sun the nine-cloud-case mean 2-D reflectance-derived plane-parallel albedo is always within 0.002 of the nine-cloud-case mean true albedo. The comparison with the IP albedo difference (not shown) demonstrates that most of the difference is caused by the negative IP bias. At the largest spatial scale the 2-D bias is positive and largest for the two cloud cases with the largest standard deviations in optical depth. These two clouds (June 17, 830 and 900) have bimodal optical depth distributions, with low-reflectance cloud sections that more fully experience the retrieval’s nonlinearity. The 2-D albedo bias for the June 8, 2000 case is artificially negative for most spatial scales, because of the maximum established value for the retrieved albedo. For a Sun angle of  $60^\circ$  the nine-cloud-case mean albedo bias is more pronounced, reaching 0.006 at the largest spatial scale, although the relative albedo error is the same as or less than that for under an overhead Sun. The larger absolute albedo bias is caused by the greater convexity of the reflectance-albedo relationship for an oblique Sun angle.

The albedo errors are very small, particularly when compared with required albedo accuracy, and lie within the radiative transfer modeling uncertainty. The relative albedo error is much smaller than the relative optical depth errors seen in Figure 11. This finding reflects a plane-parallel reflectance-albedo relationship that is more linear than its optical depth-reflectance

counterpart, rather than the reduction in albedo difference that occurs when reflectance differences are integrated over all viewing angles [*Loeb et al.*, in press, 1998]. The increased linearity also contributes to a reflectance-retrieved albedo error that is much less than the albedo error incurred in calculating the albedo from the mean optical depth (section 4).

## 8. Summary and Discussion

This paper aims to improve the conceptual understanding of 3-D radiative transfer in marine stratocumulus clouds, by applying 2-D solar radiative transfer to nine overcast stratocumulus clouds. The cloud optical properties are derived from vertically pointing NOAA K band radar observations made during ASTEX. The procedure for converting radar reflectivity to extinction is approximate, but the inferred cloud top structure is probably robust. The nine cases range from flat-topped and fairly homogeneous to thick, highly variable clouds with much cloud top topography.

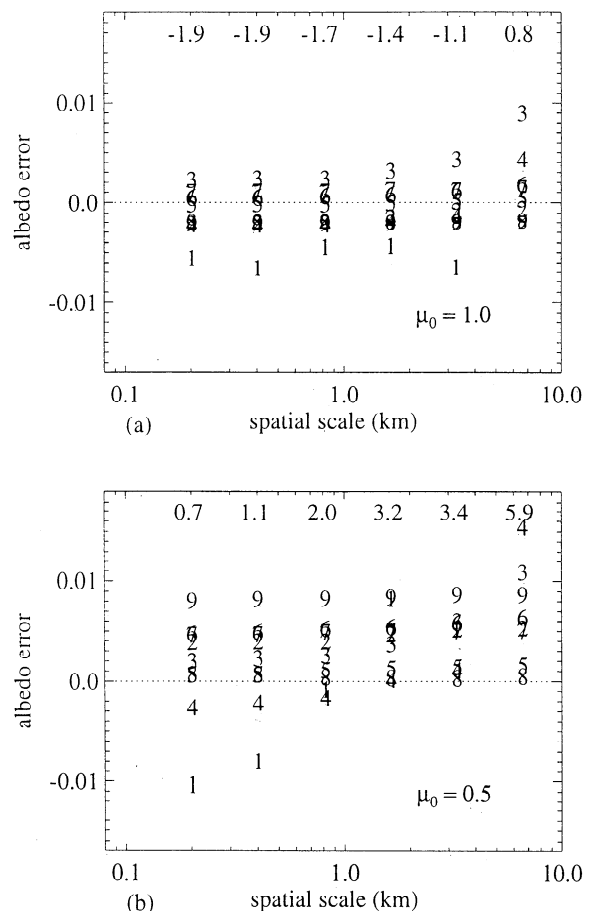


**Figure 13.** Difference between the 2-D reflectance-derived albedo and the true albedo for all nine cases as a function of spatial scale for (a) overhead Sun and (b) a solar zenith angle of  $60^\circ$ . The domain-mean difference for each cloud case is indicated by its numerical label from Table 1. The mean differences ( $\times 10^{-3}$ ) over the nine cloud cases are listed at the top.

A forward Monte Carlo model is used to calculate domain-averaged albedo for the 2-D, independent pixel, and plane-parallel approximations. As we expected, although the plane-parallel bias is significant (2% to 15%), the independent pixel bias is very small (typically under 0.003). This finding is further evidence that the independent pixel approximation is valid for domain-averaged radiative transfer in stratocumulus clouds, even when realistic vertical structure is included.

In contrast, the nadir reflectance fields can differ substantially, both in structure and in the amount of variability. To elucidate the underlying causes of variability, the spherical harmonic discrete ordinate method is applied to three constructions of the same cloud field: one is the original extinction field (2-D), while the other two have vertically uniform extinction fields but possess either a flat cloud top (UPA) or the original cloud top topography (bump). Under an overhead Sun the IPA reflectance field is consistently the "roughest", i.e., the most variable of the four possible reflectance fields. The UPA reflectances are the "smoothest", although for all nine cases the 2-D, UPA, and bump reflectances are reasonably close to each other, irrespective of the cloud top geometry. This finding is consistent with radiative smoothing being the dominant radiative process. Under a low Sun, cloud top geometry has a more pronounced impact, most noticeably for the June 8, 2000 and June 24, 1500 cases. Geometrical effects now completely overwhelm any decrease in variability caused by radiative smoothing.

Simulated retrievals of optical depths and albedos are made from the 2-D and IP reflectances to understand the effects of inhomogeneity on remote sensing retrievals. Relative albedo errors are much smaller than the optical depth errors, reflecting a plane-parallel reflectance-albedo relationship that is more linear than the reflectance-optical depth relationship. For stratocumulus clouds, plane-parallel retrievals of monochromatic albedo from near-nadir reflectances at pixel scales of 500 to 1000 m probably give a relatively unbiased estimate of albedo (under 0.005 error). At large scales the nonlinear retrieval relation is the largest contributor to both the albedo and optical depth bias, as seen by the close correspondence between the 2-D and IP biases. At small scales, geometrical effects are more important. This fact is particularly true for optical depth retrieval at low Sun angles, where the more extreme reflectances associated with substantial cloud top topography lead to a large positive bias in the retrieved optical depth.

A method is developed for empirically determining the radiance smoothing scale using the nonlocal independent pixel approximation. This smoothing scale is determined by the width of a gaussian kernel, which, when convolved with the IPA reflectance, gives the highest correlation with the 2-D reflectance. For high Sun, NIPA works quite well, indicating that diffusive radiative smoothing is the dominant horizontal transfer process. The NIPA-derived smoothing scale  $\sigma$  is about 100-

300 m (Figure 7), consistent with the radiative smoothing scale  $L = 2\pi\sigma$  of 1–2 km manifested in the power spectra of Figures 5 and 6. The empirical smoothing scale disagrees with the theoretical diffusion radiative smoothing scale of Marshak *et al.* [1995], suggesting that diffusion theory alone may not be adequate for obtaining the radiative smoothing scale for a realistic range of stratocumulus clouds.

In contrast, at low Sun, neither the power spectra nor the NIPA method reveals a radiative smoothing scale, because side illumination/shadowing effects introduce another important process that is not accounted for by NIPA. From this finding we conclude that an accurate simulation of cloud top radiance fields must include both radiative smoothing and solar beam interaction with cloud top topography. An improved technique is developed here that does include direct beam interactions with cloud geometry. This 3dbNIPA model does the direct beam flux computation in 3-D, performs the diffuse transfer on independent columns, and then applies convolution to smooth the reflectances. This approximation gives substantially higher correlation with 2-D reflectances than NIPA does for low Sun. It may be possible to improve the 3dbNIPA model even further through a diffusive-scale smoothing of the solar pseudo-source rather than of the IPA reflectances.

In this study we have examined only the radiative effects caused by the cloud top topography of overcast clouds. While these can be substantial, as seen in Figure 4, the geometry associated with a broken cloud field can produce even more pronounced radiative effects [e.g., Welch and Wielicki, 1984; Loeb and Varnai, 1997; Chambers and Wielicki, 1997]. It is our hope that the 3dbNIPA conceptual model, which includes both diffusive and direct beam geometry effects, will be applicable to the much more difficult situation of deeper broken clouds. We look forward to extending this study to this much more challenging problem.

**Acknowledgments.** This research would not have been possible without the efforts of the NOAA ETL radar group headed by Robert Kropfli. We especially thank Taneil Urtal for generous and invaluable provision of and assistance with the radar data and much useful guidance, including comments on an initial draft. The thorough and responsive comments made by three anonymous reviewers greatly improved the clarity of the document. Financial support for this research was provided by NSF Physical Meteorology grant ATM-9421733.

## References

- Albrecht, B. A., C. S. Bretherthon, and D. Johnson, Marine boundary layer structure and fractional cloudiness, *Bull. Am. Meteorol. Soc.*, 76, 889–904, 1995.
- Austin, P., Y. Wang, R. Pincus, and V. Kujala, Precipitation in stratocumulus clouds: Observational and modeling results, *J. Atmos. Sci.*, 52, 2329–2352, 1995.
- Barker, H. W., A parameterization for computing grid-averaged solar fluxes for inhomogeneous marine boundary layer clouds methodology and homogeneous biases, *J. Atmos. Sci.*, 53, 2289–2303, 1996a.



- Barker, H. W., Estimating cloud field albedo using one-dimensional series of optical depth, *J. Atmos. Sci.*, **53**, 2826–2836, 1996b.
- Barker, H. W., Broadband solar fluxes and heating rates for atmospheres with 3D broken clouds, *Q. J. R. Meteorol. Soc.*, in press, 1998.
- Cahalan, R. F., and D. Silberstein, Liquid water path and plane-parallel albedo bias during ASTEX, *J. Atmos. Sci.*, **52**, 3002–3012, 1995.
- Cahalan, R. F., W. Ridgeway, W. J. Wiscombe, T. L. Bell, and J. B. Snider, The albedo of fractal stratocumulus clouds, *J. Atmos. Sci.*, **51**, 2434–2455, 1994a.
- Cahalan, R. F., W. Ridgeway, W. J. Wiscombe, S. Gollmer, and Harshvardhan, Independent pixel and Monte Carlo estimates of stratocumulus albedo, *J. Atmos. Sci.*, **51**, 3776–3790, 1994b.
- Cess, R., et al., Absorption of solar radiation by clouds: Observations versus models, *Science*, **267**, 496–502, 1995.
- Chambers, L. H., Computation of the effects of inhomogeneous clouds on retrieval of remotely sensed properties, paper presented at the 9th Conference on Atmospheric Radiation, Am. Meteorol. Soc., Long Beach, CA, 1997.
- Chambers, L. H., and B. A. Wielicki, Independent pixel and two-dimensional estimates of Landsat-derived cloud field albedo, *J. Atmos. Sci.*, **54**, 1525–1532, 1997.
- Chambers, L. H., B. A. Wielicki, and K. F. Evans, Accuracy of the independent pixel approximation for satellite estimates of oceanic boundary layer cloud optical depth, *J. Geophys. Res.*, **102**, 1779–1794, 1997.
- Davis, A., A. Marshak, R. Cahalan, and W. Wiscombe, The Landsat scale break in stratocumulus as a three-dimensional radiative transfer effect: Implications for cloud remote sensing, *J. Atmos. Sci.*, **54**, 241–260, 1997.
- Evans, K. F., The spherical harmonic discrete ordinate method for three-dimensional atmospheric radiative transfer, *J. Atmos. Sci.*, **55**, 429–446, 1998.
- Frisch, A. S., C. W. Fairall, and J. B. Snider, Measurement of stratus cloud and drizzle parameters in ASTEX with a Ka-band Doppler radar and a microwave radiometer, *J. Atmos. Sci.*, **52**, 2788–2799, 1995.
- Gabriel, P. M., and K. F. Evans, Simple radiative transfer methods for calculating domain-averaged solar fluxes in inhomogeneous clouds, *J. Atmos. Sci.*, **53**, 858–877, 1996.
- Harshvardhan, D. A. Randall, T. G. Corsetti, and D. A. Dazlich, Earth radiation budget and cloudiness simulations with a general circulation model, *J. Atmos. Sci.*, **46**, 1922–1942, 1989.
- Hogg, D., F. Giraud, J. Snider, M. Decker, and E. Westwater, A steerable dual-channel microwave radiometer for measurement of water vapor and liquid in the atmosphere, *J. Appl. Meteorol.*, **22**, 789–906, 1983.
- Imre, D., E. Abramson, and P. Daum, Quantifying cloud-induced shortwave absorption: An examination of uncertainties and of recent arguments for large excess absorption, *J. Appl. Meteorol.*, **35**, 1991–2010, 1996.
- Kobayashi, T., Effects due to cloud geometry on biases in the albedo derived from radiance measurements, *J. Clim.*, **6**, 120–128, 1993.
- Kropfli, R. A., S. Y. Matrosov, T. Uttal, B. W. Orr, A. S. Frisch, K. A. Clark, B. W. Bartram, and J. B. Snider, Cloud physics studies with 8 mm wavelength radar, *Atmos. Res.*, **35**, 299–313, 1995.
- Loeb, N. G., and J. J. A. Coakley, Inference of marine stratus cloud optical depths from satellite measurements: Does 1D theory apply?, *J. Clim.*, in press, 1998.
- Loeb, N. G., and T. Varnai, Effect of cloud inhomogeneities on the solar zenith angle dependence of nadir reflectance, *J. Geophys. Res.*, **102**, 9387–9395, 1997.
- Loeb, N. G., T. Varnai, and D. M. Winker, Influence of sub-pixel scale cloud-top structure on reflectances from overcast stratiform cloud layers, *J. Atmos. Sci.*, in press, 1998.
- Marshak, A., A. Davis, W. Wiscombe, and R. Cahalan, Radiative smoothing in fractal clouds, *J. Geophys. Res.*, **100**, 26,247–26,261, 1995.
- Marshak, A., A. Davis, R. Cahalan, and W. Wiscombe, Non-local independent pixel and approximation: Direct and inverse problems, *IEEE Trans. Geosci. Remote Sens.*, **36**, 192–205, 1998.
- McKee, T. B., and S. K. Cox, Scattering of visible radiation by finite clouds, *J. Atmos. Sci.*, **31**, 1885–1892, 1974.
- Nakajima, T., and M. Tanaka, Algorithms for radiative intensity calculations in moderately thick atmospheres using a truncation approximation, *J. Quant. Spectrosc. Radiat. Transfer*, **40**, 51–69, 1988.
- Rossow, W. B., Measuring cloud properties from space: A review, *J. Clim.*, **2**, 201–213, 1989.
- Uttal, T., and A. S. Frisch, Cloud boundaries during ASTEX, paper presented at the 8th Conference on Atmospheric Radiation, Am. Meteorol. Soc., Nashville, Tenn., 1994.
- Welch, R., and B. Wielicki, Stratocumulus cloud field reflected fluxes: The effect of cloud shape, *J. Atmos. Sci.*, **21**, 3086–3103, 1984.
- Wielicki, B., and L. Parker, On the determination of cloud cover from satellite sensors: The effect of sensor spatial resolution, *J. Geophys. Res.*, **97**, 12,799–12,823, 1992.

K. F. Evans and P. Zuidema, Program in Atmospheric and Oceanic Sciences, Campus Box 311, University of Colorado, Boulder, CO 80309. (e-mail: evans@nit.colorado.edu; zuidema@monsoon.colorado.edu)

(Received September 26, 1997; revised December 24, 1997; accepted December 30, 1997.)